# Synthesis of cyclo[18]carbon *via* debromination of $C_{18}Br_6$

Lorel M. Scriven,[a]† Katharina Kaiser,[b]† Fabian Schulz,[b,c] Alistair J. Sterling,[a]

Steffen L. Woltering,[a] Przemyslaw Gawel,[a] Kirsten E. Christensen,[a] Harry L. Anderson,[a]*

and Leo Gross[b]*

[a] Department of Chemistry, Oxford University, Chemistry Research Laboratory, Oxford, OX1 3TA, United Kingdom.

[b] IBM Research–Zurich, Säumerstrasse 4, 8803 Rüschlikon, Switzerland.

[c] Present address: Fritz Haber Institute of the Max Planck Society, Faradayweg 4-6, 14195 Berlin, Germany

† These authors contributed equally.

## Table of Contents
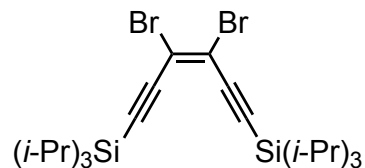
## Section 1: Materials and Methods

Reagents (Alfa Aesar, Aldrich, Acros, Fluorochem, Fisher Scientific) were used without further purification. Dry solvents (THF, toluene, $CH_2Cl_2$) for reactions were purified by a MBraun MB-SPS-5-Bench Top under nitrogen ($H_2O$ content < 20 ppm). All other solvents used were HPLC grade. Reactions, unless otherwise stated, were carried out in oven-dried glassware under a $N_2$ atmosphere. Flash column chromatography was carried out on a Biotage Isolera One with a 200–400 nm UV detector. Analytical thin layer chromatography (TLC) were performed on aluminium sheets coated with silica gel 60 F254 (Merck). UV light (254 nm) was used for visualization. Evaporation *in vacuo* was performed at 15–40 °C and 5–1010 mbar. Reported yields refer to pure compounds dried under high vacuum (< 0.1 mbar). $^1H$ and $^{13}C$ nuclear magnetic resonance (NMR) were recorded on Bruker AVIII HD 400 spectrometer at 400 MHz ($^1H$) and 101 MHz ($^{13}C$) at 294 K. Chemical shifts, δ, reported in ppm downfield from tetramethylsilane using residual deuterated solvent signals as internal reference ($CDCl_3$: $δ_H$ = 7.26 ppm, $δ_C$ = 77.16 ppm). High-resolution mass spectrometry (HR-MS) measurements were performed by the mass spectrometry service at the University of Oxford on a Waters GTC classic. Differential scanning calorimetry was carried out on a Perkin Elmer DSC 4000. Analytical gel permeation chromatography (GPC) was carried out on a VWR system with a JAIGEL H-P pre-column, a JAIGEL 4H-A column (8 mm x 500 mm) in series with THF/1% pyridine containing 0.1% BHT stabilizer as the eluent with a flow rate of 1 mL/min. Bis(tri-*iso*-propylsilyl)hexatriyne **1** was synthesized using published procedures.[1-3]

## Section 2: Synthetic Procedures

### Synthesis of compound 3

Bis(tri-*iso*-proylsilyl)hexatriyne **1** (5.14 g, 13.3 mmol), Pt(PPh$_3$)$_4$ (496 mg, 0.40 mmol) and bis(pinacolato)diboron (3.71 g, 14.6 mmol) were dissolved in dry toluene (26 mL) under $N_2$ and the clear orange solution was freeze-pump-thaw degassed. The solution was then heated to 100 °C for 90 h. The solvent was removed *in vacuo* to yield crude **2** as an orange oil that was unstable to silica and thus the crude was carried through to the next step without further purification. $^1$**H NMR** (400 MHz, CDCl$_3$): $δ_H$ = 1.29 (24H, s; bpin), 1.10 (s, 42H; TIPS) ppm. $^{13}$**C NMR** (101 MHz, CDCl$_3$): $δ_C$ = 107.7, 103.4, 84.3, 83.1, 24.8, 18.8, 11.4 ppm. **IR** (ATR): $\tilde{v}$ = 633, 660, 674, 695, 756, 811, 850, 882, 923, 971, 996, 1062, 1144, 1214, 1271, 1332, 1358, 1462, 1535, 2130, 2865, 2942 cm$^{-1}$.

Copper(II) bromide (17.8 g, 79.7 mmol) was added to a solution of the crude **2** in THF (45 mL) and water (30 mL). The resulting dark brown solution was heated to 70 °C with a reflux condenser for 18 h. An additional aliquot of CuBr$_2$ (6.0 g, 26.9 mmol) in THF (20 mL) was added and the reaction heated to 80 °C for an additional 20 h. The reaction was monitored by NMR and quenched upon loss of the bpin signal in the crude NMR. Upon completion of the reaction the solution was diluted with water (50 mL) and extracted with diethyl ether (3 × 50 mL) and the organic phase dried over MgSO$_4$. The crude was purified by column chromatography, SiO$_2$ (petroleum ether) to yield **3** as a red oil (3.84 g, 53% from **1**). $^1$**H NMR** (400 MHz, CDCl$_3$): $δ_H$ = 1.04 (s, 42H; TIPS) ppm. $^{13}$**C NMR** (101 MHz, CDCl$_3$): $δ_C$ = 112.2, 105.1, 102.7, 18.8, 11.3 ppm. **HR-APCI-MS**: *m/z* = 547.1246 (calc *m/z* C$_{24}$H$_{43}$Br$_2$Si$_2$$^+$: 547.1245). **IR** (ATR): $\tilde{v}$ = 619, 664, 678, 818, 883, 920, 997, 1018, 1042, 1176, 1242, 1367, 1384, 1463, 2137, 2866, 2891, 2943 cm$^{-1}$.
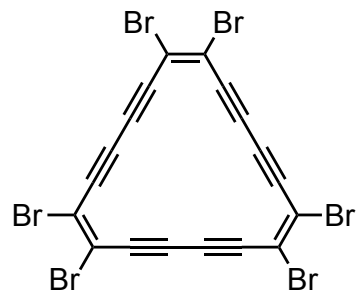
**Synthesis of C$_{18}$Br$_6$**

Tetrabutylammonium fluoride (1.61 mL, 1.0 M in THF, 1.61 mmol) was added to a solution of compound **3** (400 mg, 0.73 mmol) in THF (25 mL) and water (0.25 mL) at 0 °C. The resulting clear orange solution was stirred and monitored by TLC until the reaction had reached completion, approximately 1.5 h. Water (25 mL) was added and the aqueous phase was extracted with Et$_2$O (2 × 20 mL) and dried over MgSO$_4$. The crude was purified by column chromatography, SiO$_2$ (petroleum ether) to yield **4** as a yellow solution in petroleum ether (2 mL) that was diluted with dry CH$_2$Cl$_2$ for use directly in the next step. **$^1$H NMR** (400 MHz, CDCl$_3$): $\delta_H$ = 3.75 (s, 2H) ppm. **$^{13}$C NMR** (101 MHz, CDCl$_3$): $\delta_C$ = 112.9, 87.6, 80.2 ppm. **GC-EI-MS**: $m/z$ = 231.8523 (calc $m/z$ C$_6$H$_2$Br$_2^+$: 231.8518).

The Glaser-Hay catalyst was prepared by addition of TMEDA (0.12 mL, 0.81 mmol) to a solution of CuCl (189 mg, 1.91 mmol) in dry CH$_2$Cl$_2$ (1.9 mL) under N$_2$. The resulting pale green suspension was stirred for 30 min and then allowed to settle, and 0.39 mL of the supernatant solution was withdrawn and added to the vigorously stirred solution of **4** in dry CH$_2$Cl$_2$ (50 mL) under O$_2$. An immediate color change was observed after addition of the catalyst from clear yellow to deep red. An insoluble brown precipitate slowly formed over the course of the reaction. The mixture was stirred for 48 h and the end point was determined by consumption of the starting material, determined by TLC analysis. (**Note:** The crude reaction mixture from this cyclization reaction was found to be explosive if scratched. Care should be taken to work on a small scale. Monomer **4** should not be fully dried and non-flammable solvents used where possible.)

The reaction mixture was diluted with CH$_2$Cl$_2$ (200 mL) and washed with water (200 mL). A brown emulsion was formed in the aqueous layer, which was extracted with CH$_2$Cl$_2$ (2 × 200 mL) until all brown emulsion had been removed from the pale blue aqueous layer. The organic layer was combined, washed with water (500 mL) and dried over MgSO$_4$ to yield a clear orange solution. The solution was concentrated to approximately 10 mL and diluted with petroleum ether (350 mL) to form a dark brown solution, which was filtered through a SiO$_2$ plug to yield a clear yellow solution. This solution was concentrated to approximately 20 mL and a red insoluble solid formed which stuck to the sides of the flask. The solution was diluted with CHCl$_3$ (100 mL) and sonicated to suspend the red solid in solution, the solution was then concentrated again to approx. 10 mL to give a red solid suspended in an orange solution, the red solid was collected using syringe filtration. Analytical GPC analysis revealed the red solid to be predominantly **C$_{18}$Br$_6$** with some slightly larger species. The crude was triturated with CH$_2$Cl$_2$ (25 mL) and then washed with pentane (25 mL) to yield **C$_{18}$Br$_6$** as a bright red crystalline solid (6.0 mg, 4% from **3**). Crystalline material suitable for X-ray diffraction was obtained by cooling of a saturated solution of **C$_{18}$Br$_6$** in CS$_2$ to 4 °C for 4 days to yield red parallelepipeds. **C$_{18}$Br$_6$: M.p.:** decomposes to black solid around 145 °C, no further change seen up to 300 °C. **$^1$H NMR** (400 MHz, CDCl$_3$): no signals. **$^{13}$C NMR** (101 MHz, CDCl$_3$): too insoluble to obtain. **HR-APCI-MS**: $m/z$ = 689.2725 (mass corresponds to C$_{18}^{79}$Br$_6^-$, $m/z$: 689.5106), 691.5077 (calc $m/z$ C$_{18}^{79}$Br$_5^{81}$Br$^-$: 691.5086), 693.5058 (calc $m/z$ C$_{18}^{79}$Br$_4^{81}$Br$_2^-$: 693.5065), 695.5035 (calc $m/z$ C$_{18}^{79}$Br$_3^{81}$Br$_3^-$: 695.5046), 697.5015 (calc $m/z$ C$_{18}^{79}$Br$_2^{81}$Br$_4^-$: 697.5026), 699.4994 (calc $m/z$ C$_{18}^{79}$Br$^{81}$Br$_5^-$: 699.5007), 701.4978 (calc $m/z$ C$_{18}^{81}$Br$_6^-$: 701.4986). **UV/vis** (CHCl$_3$): $\lambda_{max}$ ($\varepsilon$) = 416 (13808), 403 (26114), 362 (52239), 347 (35154), 340 (31695), 265 (32394), 253 (33143 M$^{-1}$ cm$^{-1}$). **IR (ATR)**: $\tilde{v}$ = 2112 (weak C≡C), 1048, 872, 858 cm$^{-1}$.

## Section 3: Differential Scanning Calorimetry of $C_{18}Br_6$

Differential scanning calorimetry was carried out on 0.6 mg of $C_{18}Br_6$ which was sealed into an aluminum pan and heated relative to an empty reference (Fig. S1). The sample was held for 1 minute at 50 °C, heated from 50 °C to 250 °C at 10 °C/min, held for 1 minute at 250 °C and then cooled from 250 °C to 50 °C at 10 °C/min. A large exotherm was observed during the heating cycle, from 85 °C to 125 °C, corresponding to an enthalpy of $\Delta H = -109$ kJ/mol. An additional scan was then carried out on the same sample and no further exotherms were observed, presumably due to decomposition of the sample.
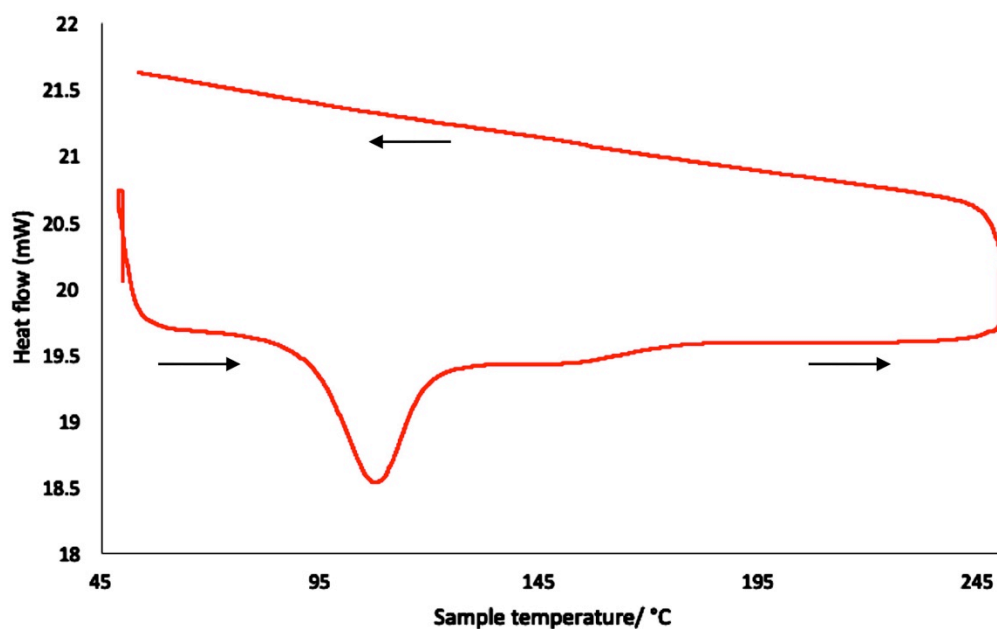


**Figure S1.** DSC curve of $C_{18}Br_6$ with a heating rate of 10 °C/min.

## Section 4: X-Ray Crystallography

Crystals of $C_{18}Br_6$ were obtained by cooling of a saturated solution of in $CS_2$ to 4 °C for 4 days. Single crystal X-ray diffraction data were collected using a Rigaku Oxford Diffraction SuperNova diffractometer fitted with an Oxford Cryosystems Cryostream 700 plus open flow nitrogen cooling device.[4] The CrysAlisPro software was used for data collection and integration. The structure was solved using SHELXT[5] within the CRYSTALS suite.[6] The structures were then modified, improved and optimised by full-matrix least squares on $F^2$ as per the CIF.

Crystallographic data have been deposited with the Cambridge Crystallographic Data Centre (CCDC 1998472) and can be obtained via www.ccdc.cam.ac.uk/data_request/cif.

## Section 5: Scanning Probe Microscopy

The STM and AFM measurements were carried out in a home-built combined STM/AFM setup, at a base pressure of $p \approx 10^{-11}$ mbar and a temperature of $T \approx 5$ K, equipped with a qPlus force sensor[7] operating in frequency-modulation mode.[8] The single-crystalline Cu(111) substrate was cleaned by *in situ* sputtering and annealing cycles and partially covered with bilayer NaCl (NaCl(2ML)/Cu(111)),[9–10] which was prepared by sublimation of NaCl onto the clean Cu(111) surface held at ~5 °C. The precursor molecules were thermally sublimed onto the cold NaCl(2ML)/Cu(111), yielding a sub-monolayer coverage of well-dispersed molecules. Carbon monoxide (CO) was used for tip functionalization. To that end gaseous CO was allowed into the chamber up to a partial pressure of $6 \times 10^{-8}$ mbar. Subsequently, the shutter to the microscope was opened for 20 s. For functionalization, CO was picked up from bilayer NaCl.[11,12]

## Section 6: On-surface Synthesis of Cyclo[18]carbon and Reaction Statistics

For the on-surface formation of cyclo[18]carbon from $C_{18}Br_6$, the tip was positioned in the vicinity of a precursor molecule, retracted a few Å from the STM set-point (usually $I = 0.5$ pA, $V = 0.2$ V) and the sample voltage $V$ was increased for a few seconds. Debromination was possible at both bias polarities but was found to be more successful at positive sample voltages. The voltage threshold for debromination at positive voltage polarity was found to be around 1.2 V and dissociation of single bromine atoms already occurred before reaching the negative ion resonance of the precursor molecule. Debromination was found to be most successful for lateral distances between tip and precursor molecule of 1–3 nm, relatively large tip-sample distances (tip retracted by 2–3 Å from the STM set-point, *i.e.*, $I < 50$ fA) and sample voltages of around 2 V. In most cases, this procedure resulted in the dissociation of less than 6 Br from the precursor. Two examples of observed intermediates are shown in Fig. S2a and b. However, for intermediate molecules it was often not possible to determine the exact number of dissociated Br atoms from AFM images as they often stayed next to the intermediate and obscured the contrast in their vicinity. When we observed the characteristic nine-fold symmetric contrast of $C_{18}$, we concluded that all six Br were dissociated. Table S1 summarizes the outcome of all tip-induced debromination attempts starting from the intact precursor or an intermediate. The total on-surface reaction yield for cyclo[18]carbon formation was 64.3%, *i.e.*, in 64% of the cases we generated $C_{18}$ from an intact $C_{18}Br_6$ precursor by applying one or more successive voltage pulses, and in 36% we generated another final product.

**Table S1.** Reaction statistics for on-surface debromination of $C_{18}Br_6$. Educts were the intact precursor and partially debrominated intermediates. Reaction products were cyclo[18]carbon ($C_{18}$), partially debrominated intermediates (Fig. S2a, b), chain-like structures due to breaking of a bond within the cyclic system (non-cyclic products, Fig. S2c) and other rare cyclic reaction products that could not be further manipulated (rare final products, Fig. S2d). A total of 21 single molecule reactions induced by atom manipulation were evaluated.

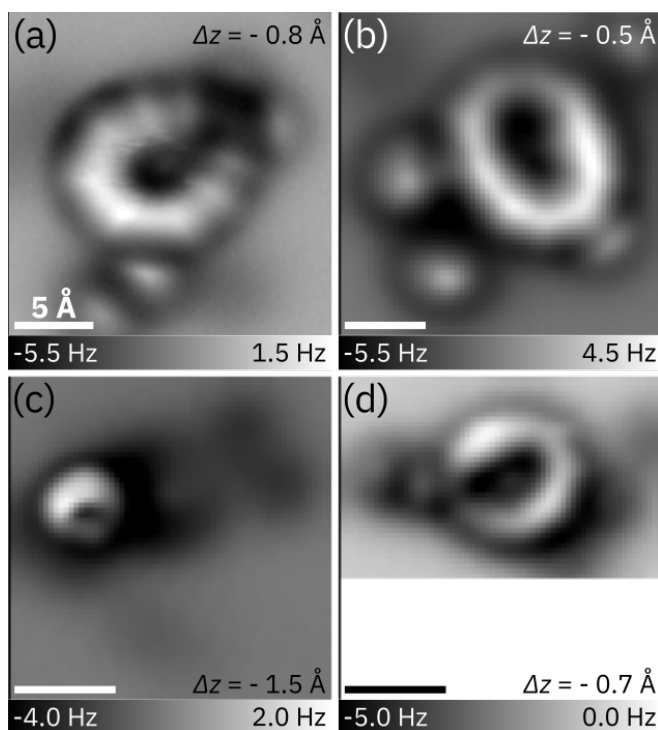| Product / Educt | $C_{18}$ | intermediates | non-cyclic products | rare final products |
|---|---|---|---|---|
| $C_{18}Br_6$ | 21.4% | 42.9% | 7.1% | 28.6% |
| intermediate | 100% | | | |

**Figure S2**. AFM images of different reaction products generated *via* atom manipulation of $C_{18}Br_6$. (a) and (b) show intermediates with at least four Br masking groups already dissociated. (c) shows a non-cyclic product and (d) a rare final product. $\Delta z$ denotes the tip-height offset from an STM set-point of $I = 0.5$ pA, $V = 0.2$ V. All scale bars correspond to 5 Å.
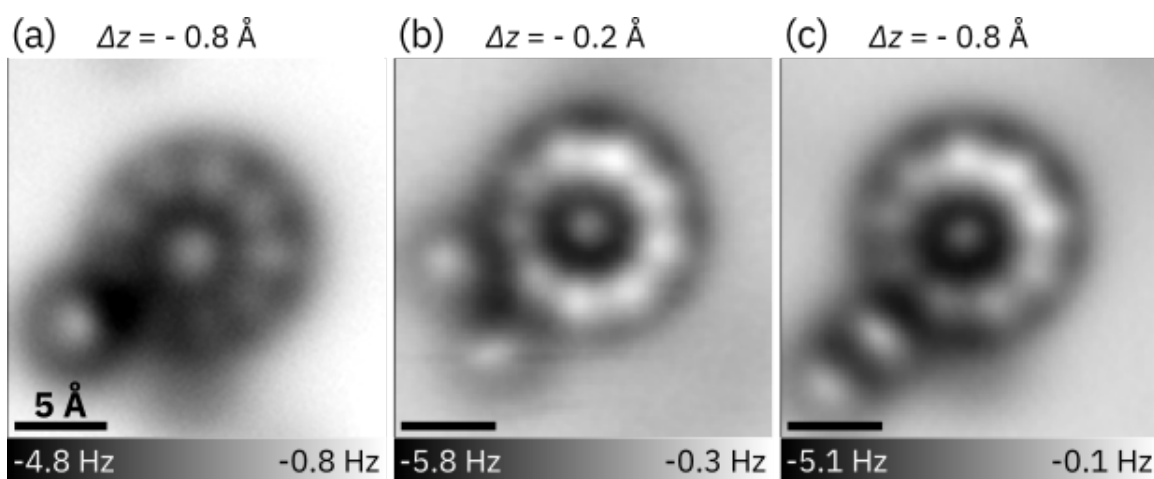


**Figure S3**. AFM images of different $C_{18}$ molecules generated by atom manipulation of $C_{18}Br_6$. The bright features next to the molecules can be assigned to dissociated Br atoms. $\Delta z$ denotes the tip-height offset from an STM set-point of $I = 0.5$ pA, $V = 0.2$ V. All scale bars correspond to 5 Å.
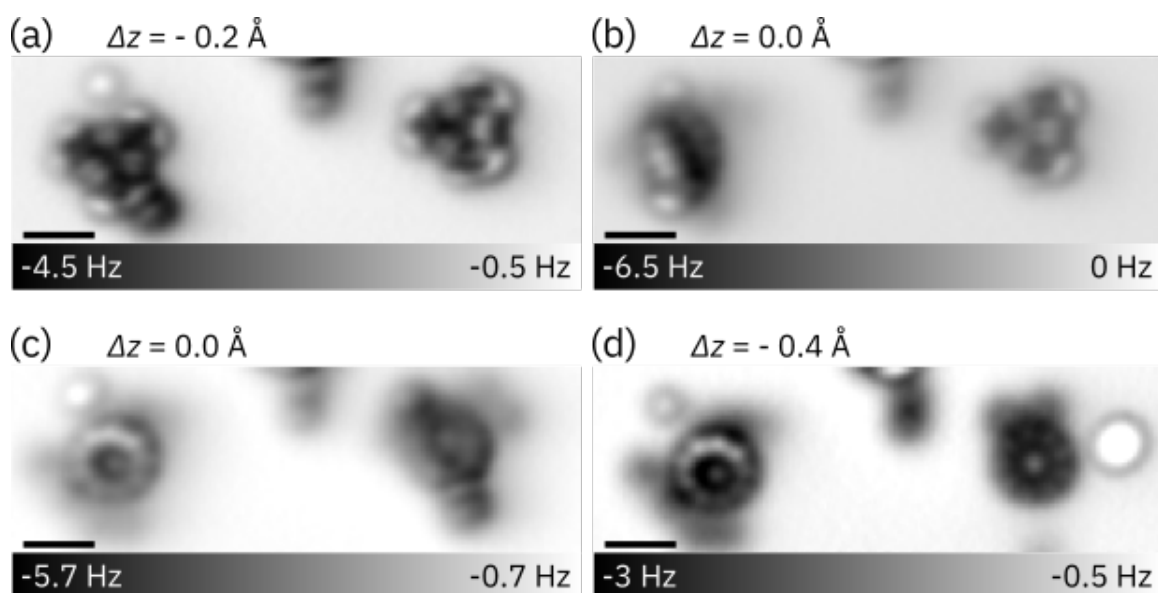
**Figure S4**. AFM images of two $C_{18}Br_6$ precursors prior to and after applying bias voltage pulses of 2–3 V with the tip positioned in proximity to the molecules. (a) Shows both intact precursors prior to atom manipulation. In (b), the precursor on the left has reacted to an intermediate while the precursor on the right remained intact. In (c) the precursor on the left has reacted to $C_{18}$ and the precursor on the right has reacted to an intermediate. (d) Shows two cyclo[18]carbon molecules generated by atom manipulation from the precursors shown in (a). The dark features next to the molecules can be assigned to dissociated Br atoms. They hinder motion of the molecules such that the intermediates and cyclo[18]carbon molecules are held in place during voltage pulsing. $\Delta z$ denotes the tip-height offset from an STM set-point of $I = 0.5$ pA, $V = 0.2$ V. All scale bars correspond to 5 Å.

## Section 7: Reaction Mechanism of Debromination

As we observed several partly debrominated reaction intermediates (see Fig. S2 and Fig. S4), we conclude that the debromination of $C_{18}Br_6$ occurs in several steps. Dissociated Br atoms are often observed as individual Br atoms on the NaCl surface near the molecule (see, *e.g.*, Fig. S3). Because the debromination can be induced even with the tip laterally displaced a few nanometers from the molecule, we assume that the reaction is mediated by hot interface state charge carriers. The bond is likely broken by inelastic energy transfer from charge carriers to the molecule.[13,14] Surface state charge carriers have been shown to induce nonlocal reactions on Cu(111).[15,16] The Cu(111) surface state survives as an interface state for bilayer NaCl on Cu(111).[10] Interface-state charge carriers have been proposed to mediate halogen dissociation reactions[17] and unmasking of the $C_{24}O_6$ precursor of cyclo[18]carbon[18] on bilayer NaCl on Cu(111).

In a preceding study, we investigated the stepwise debromination of a dibromo-alkene on Cu(111) as a function of bias voltage and tunnel current.[19] We concluded a single-electron process for both Br dissociation reactions. In the present study of $C_{18}Br_6$ on NaCl bilayer on Cu(111), a quantification of the electron yield and determination of the voltage thresholds for the individual debromination reactions was not feasible, because the bias threshold does not increase for successive reaction steps,

many different intermediates are possible after a pulse and the assignment of the intermediates is challenging (see Fig. S2).

For $C_{18}Br_6$ on bilayer NaCl on Cu(111), our observations and comparison with previous results[17-19] point towards successive debromination reactions, induced stepwise by single electrons with a voltage threshold of 2 V or less for each individual C-Br dissociation. For the first Br dissociation from $C_{18}Br_6$ the voltage threshold was about 2 V. Because of the observation that we often dissociated several Br within one 2 V voltage pulse until we formed $C_{18}$, we conclude that the debromination reactions after the first debromination exhibit voltage thresholds of approximately 2 V or less. However, for these subsequent Br dissociations, we cannot exclude that some of them occur spontaneously or that their bias threshold is significantly smaller than 2 V.

Note that our reported yield for generating $C_{18}$ from the $C_{18}Br_6$ precursor on the surface by atom manipulation does not consider the yield for preparing the precursors on the NaCl/Cu(111) surface (preparation yield). When subliming $C_{18}Br_6$ from the wafer, a large fraction is not directed towards the sample, and from the molecules adsorbed on the sample only those on NaCl islands can be used to generate $C_{18}$. Also, we cannot exclude that a fraction of the precursor molecules react when we apply them onto the wafer, as the precursor is a shock-sensitive explosive. For sublimation from the wafer, we heated the wafer from room temperature to 900 K within a few seconds, because a steep temperature ramp is usually beneficial to increase the ratio of desorption versus fragmentation.[20,21] However, we cannot exclude that a fraction of the precursors fragments and/or reacts (*e.g.* polymerizes) on the wafer in this sublimation step of the sample preparation.

### Section 8: Simulation of AFM Images

AFM images of the different calculated geometries of cyclo[18]carbon were simulated using the Probe-Particle Model (PPM) implemented by Hapala *et al.*[22] In this code, the interaction between (functionalized) tip and sample is calculated using classical force fields to determine the relaxation of the probe particle (CO) in the presence of the molecule. Electrostatic interactions between the CO at the tip apex and the molecule are modelled by assigning a charge and charge distribution to the CO and calculating its interactions with the Hartree potential of the molecule. For the simulations we used an oscillation amplitude of $A = 50$ pm, a lateral spring constant of the CO of 0.2 N/m and an electrostatic monopole on the oxygen of –0.05 e.[18,23]

As input for the AFM simulations we used the atomic coordinates from high level *ab initio* CCSD calculations,[24] as well as related coordinates with up to a factor of four increase in the BAA.
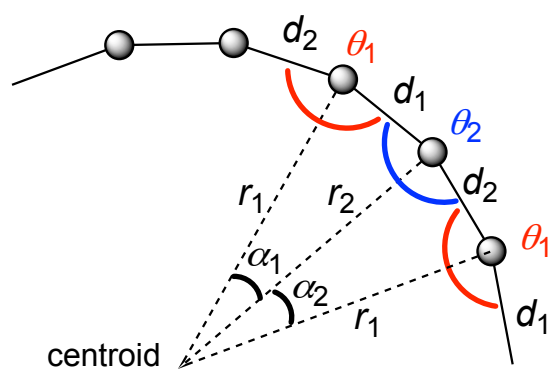


**Figure S5.** Definition of the radial coordinates $r_1$, $r_2$, $\alpha_1$ and $\alpha_2$ for a molecule of $C_{18}$ ($\alpha_1 + \alpha_2 = 40°$).

Polar atomic coordinates, $r_1$, $r_2$, $\alpha_1$ and $\alpha_2$ were calculated from bond lengths $d_1$ and $d_2$ and bond angles $\theta_1$ and $\theta_2$ using equations S1–S4:

$$r_1 = \frac{\sqrt{d_1^2 + d_2^2 - d_1 d_2 \cos \theta_1}}{2 \sin(20°)} \tag{S1}$$

$$r_2 = \frac{\sqrt{d_1^2 + d_2^2 - d_1 d_2 \cos \theta_2}}{2 \sin(20°)} \tag{S2}$$

$$\alpha_1 = \cos^{-1}\left(\frac{r_1^2 + r_2^2 - d_1^2}{2 r_1 r_2}\right) \tag{S3}$$

$$\alpha_2 = \cos^{-1}\left(\frac{r_1^2 + r_2^2 - d_2^2}{2 r_1 r_2}\right) \tag{S4}$$

The corresponding Hartree potentials were calculated using the all-electron density functional theory (DFT) code FHI-aims[25] by letting the electronic structure relax while constraining the atomic coordinates. The same settings as in ref. 24 were used. We used the Heyd-Scuseria-Ernzerhof (HSE) hybrid functional[26] as the exchange-correction functional, with a mixing parameter of 0.8. The Tkatchenko-Scheffler correction[27] was used to account for van der Waals interactions. For all calculations the default 'tight' settings for the atomic basis set were used. From the tip-height offsets $\Delta z$ of the simulated AFM images a constant was subtracted, so that the $\Delta z$ of the simulations approximately correspond to the experimental data.

The simulated AFM images of cyclo[18]carbon with a $D_{18h}$ cumulene geometry (Fig. S6) show a uniform circular shape, without contrast modulations for all tip-sample distances. Fig. S7 shows simulated AFM images of the $D_{9h}$ polyyne geometry with the BLA theoretically predicted in ref. 24 (Fig. S7b) as well as geometries with half (Fig. S7a) and twice (Fig. S7c) this predicted BLA. The AFM simulations of the different $D_{9h}$ polyyne geometries illustrate how the AFM contrast evolves with different BLA: The differences in the $\Delta f$ signal between the neighboring single and triple bonds in cyclo[18]carbon relate to their respective differences in electron density. The larger the BLA, the greater are the differences in electron density between formal single and triple bonds (bond order alternation) and thus, the more pronounced are the differences in the AFM contrast above single and triple bonds. In agreement with this, the bright lobes atop the triple bonds in the AFM simulations at large tip-sample distances (0.8 Å $\geq \Delta z \geq$ 0.5 Å) are most pronounced in Fig. S7c (largest BLA) and least pronounced in Fig. S7a (smallest BLA). With the parameters that we used in the PPM simulations, Fig. S7b fits best to our experimental data.

Figure S8a–c shows simulated AFM images of the $D_{9h}$ cumulene geometry with different degrees of BAA. AFM simulations of the theoretically predicted geometry from ref. 24 with bond angles of $\theta_1 =$ 162.85° and $\theta_2 =$ 157.15° (BAA = 5.7°) are shown in Fig. S8a. The simulated AFM images are almost identical to those of the $D_{18h}$ cumulene geometry (Fig. S6). For twice the theoretically predicted BAA (11.4°), the changes in the bond angles become apparent as corners in the AFM simulations for small $\Delta z$ (Fig. S8b). However, at larger $\Delta z$ the contrast still resembles that of the $D_{18h}$ geometry. For the BAA of 22.8° (Fig. S8c) a nine-fold symmetry is already visible at large $\Delta z$, i.e., $\Delta z =$ 0.7 Å, where corners

can be seen. In contrast to the polyyne geometries, the magnitude of the $\Delta f$ contrast is uniform above the ring. Interestingly, the simulations at small tip-sample distances, *i.e.*, $\Delta z = 0.1$ Å and $\Delta z = 0.2$ Å, are very similar to the contrast of the polyyne geometries exhibiting a nonagon, although the origin of the nonagonal contrast is quite different for cumulene and polyyne. In the $D_{9h}$ polyyne, the nonagonal shape arises because of the different electron densities above single and triple bonds and the corners of the nonagon are located above the positions of triple bonds. In $D_{9h}$ cumulenes, the nonagon relates to the geometry of the molecule and the corners are located above the atom positions at more acute bond angles.

Figure S9 shows simulated AFM images of the $C_{9h}$ polyyne geometry with different magnitude of BAA. The theoretically predicted geometry from ref. 24 with bond angles of $\theta_1 = 163.27°$ and $\theta_2 = 156.73°$ is shown in Fig. S9a. Geometries with twice and four times the BAA are shown in Fig. S9b,c, respectively. The AFM simulations of all three geometries show nine-fold symmetry with bright lobes atop the triple bonds at larger tip-sample distances (0.8 Å $\geq \Delta z \geq$ 0.4 Å) that transition into corners for smaller $\Delta z$, similar to the $D_{9h}$ geometry. At larger tip-sample distances (0.8 Å $\geq \Delta z \geq$ 0.5 Å) the lobes appear slightly asymmetric (droplet-shaped rather than oval), with the larger end pointing towards the more acute bond angle, reflecting the prochirality of the molecule. The $C_{9h}$ geometries with different BAA look very similar in the simulated AFM images.
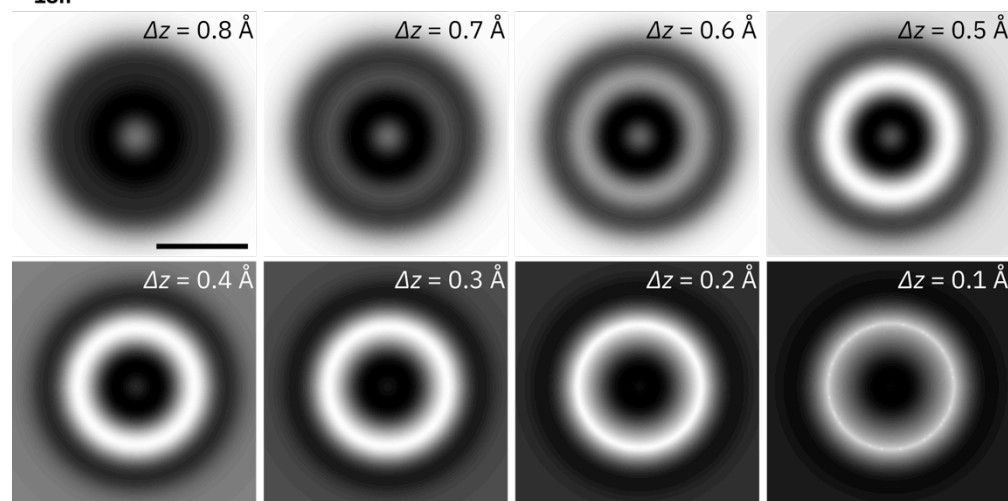
## D$_{18h}$ cumulene



**Figure S6.** Calculated AFM images of $C_{18}$ with a $D_{18h}$ cumulene geometry at decreasing tip-sample distances from top left to bottom right (geometry **A**: $d_1 = d_2 = 1.297$ Å, $\theta_1 = \theta_2 = 160°$).

**D$_{9h}$ polyyne**

(a)

$d_1 = 1.274$ Å

$d_2 = 1.347$ Å



(b)

$d_1 = 1.238$ Å

$d_2 = 1.383$ Å
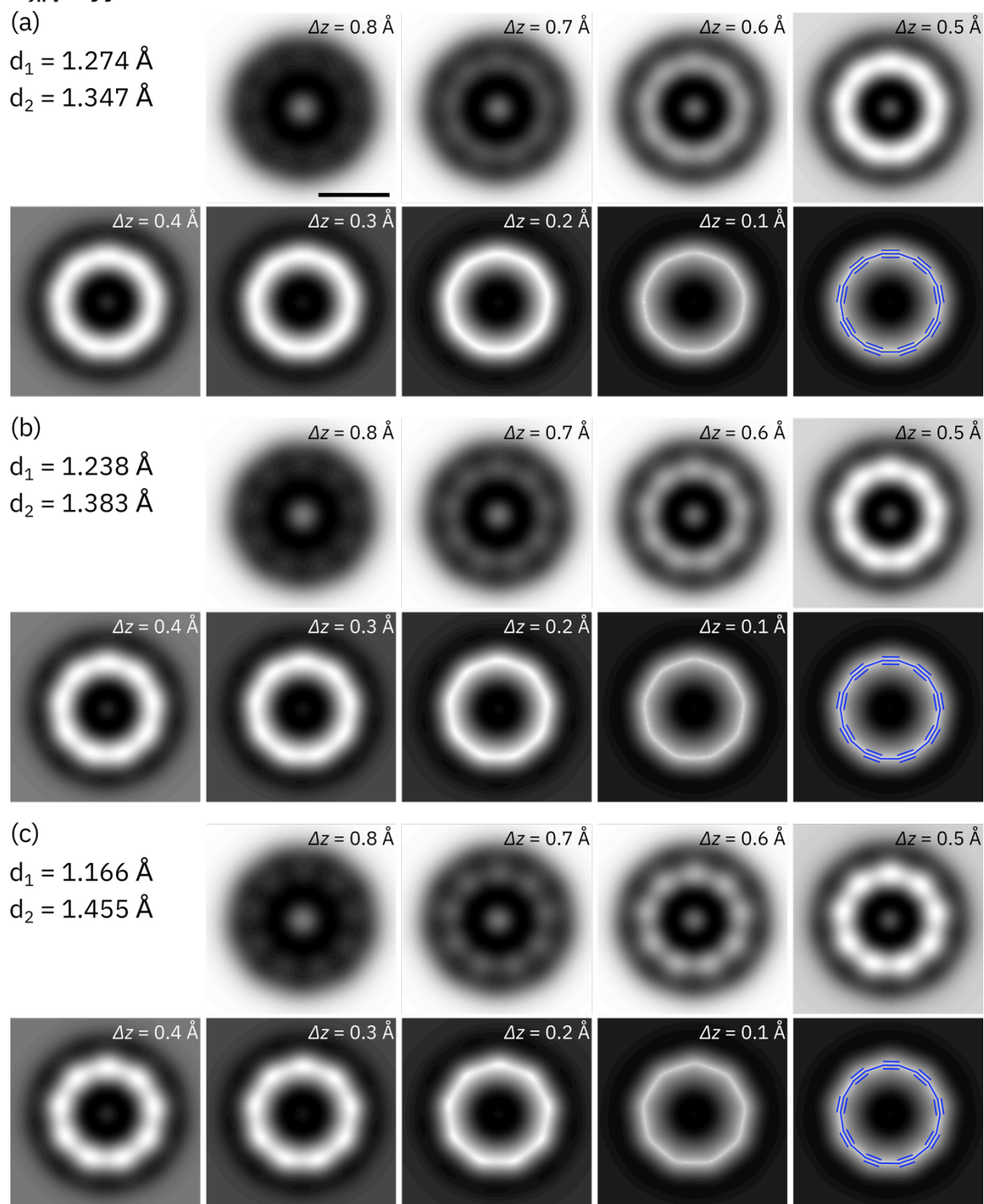


(c)

$d_1 = 1.166$ Å

$d_2 = 1.455$ Å



**Figure S7.** Calculated AFM images of $C_{18}$ with a $D_{9h}$ polyyne geometry with different degrees of BLA at decreasing tip-sample distances from top left to bottom right. The BLA corresponds to half the theoretically predicted value (**a**, BLA = 0.073 Å), the predicted geometry of ref [24] (**b**, BLA = 0.145 Å) and twice the predicted value (**c**, BLA = 0.289 Å). The images in the respective bottom right panels show again the AFM simulation for $\Delta z = 0.1$ Å, but overlaid with the corresponding molecular structure model.
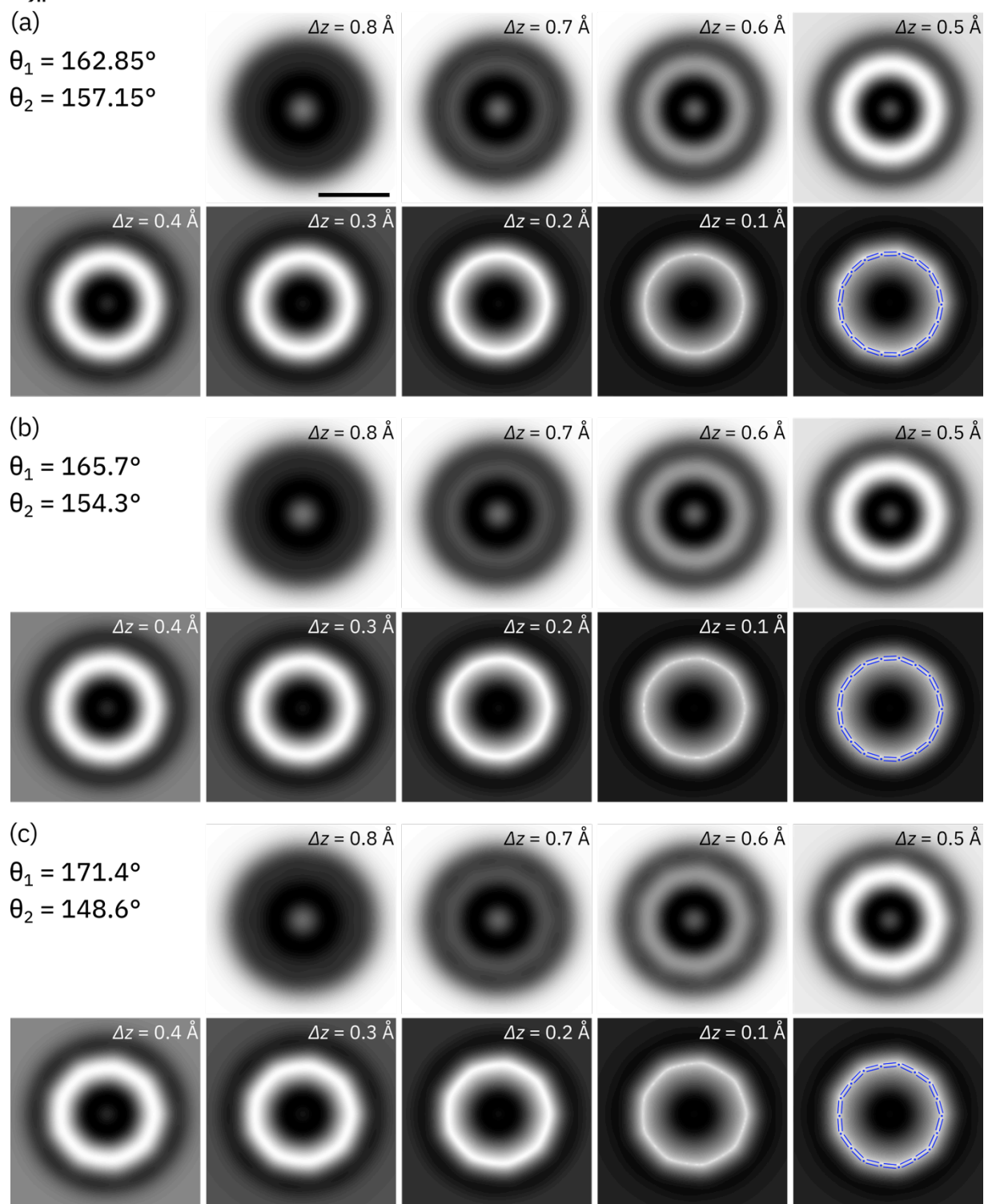
**D$_{9h}$ cumulene**

(a)

$\theta_1 = 162.85°$

$\theta_2 = 157.15°$



(b)

$\theta_1 = 165.7°$

$\theta_2 = 154.3°$



(c)

$\theta_1 = 171.4°$

$\theta_2 = 148.6°$



**Figure S8.** Calculated AFM images of C$_{18}$ with a $D_{9h}$ cumulene geometry with different degrees of BAA at decreasing tip-sample distances. The BAA corresponds to the calculated geometry of ref [24] (**a**, BAA = 5.7°) as well as twice (**b**, BAA = 11.4°) and four times the theoretically predicted value (**c**, BAA = 22.8°). The images in the respective bottom right panels show again the AFM simulation for $\Delta z$ = 0.1 Å, but overlaid with the corresponding molecular structure model.

**C$_{9h}$ polyyne**

(a)

$\theta_1 = 163.27°$
$\theta_2 = 156.73°$

(b)

$\theta_1 = 166.54°$
$\theta_2 = 153.46°$

(c)

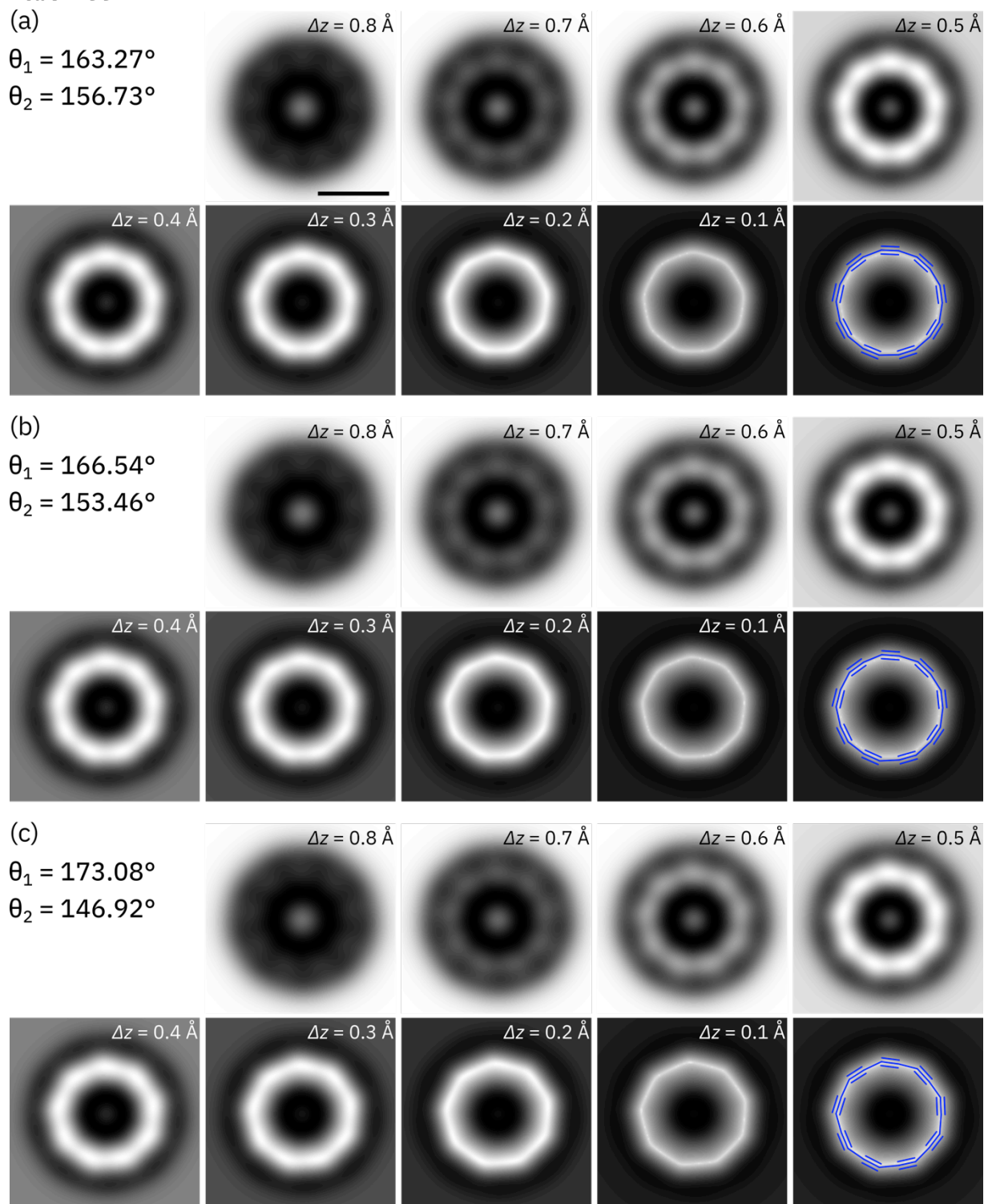$\theta_1 = 173.08°$
$\theta_2 = 146.92°$

**Figure S9.** Calculated AFM images of C$_{18}$ with a $C_{9h}$ polyyne geometry with different degrees of BAA at decreasing tip-sample distances from top left to bottom right. The BAA corresponds to the calculated geometry of ref [24] (**a**, BAA = 6.54°) as well as twice (**b**, BAA = 13.08°) and four times this value (**c**, BAA = 26.16°). The images in the respective bottom right panels show again the AFM simulation for $\Delta z = 0.1$ Å, but overlaid with the corresponding molecular structure model.

## Section 9: Selected NMR and Mass Spectra

Compound **2**

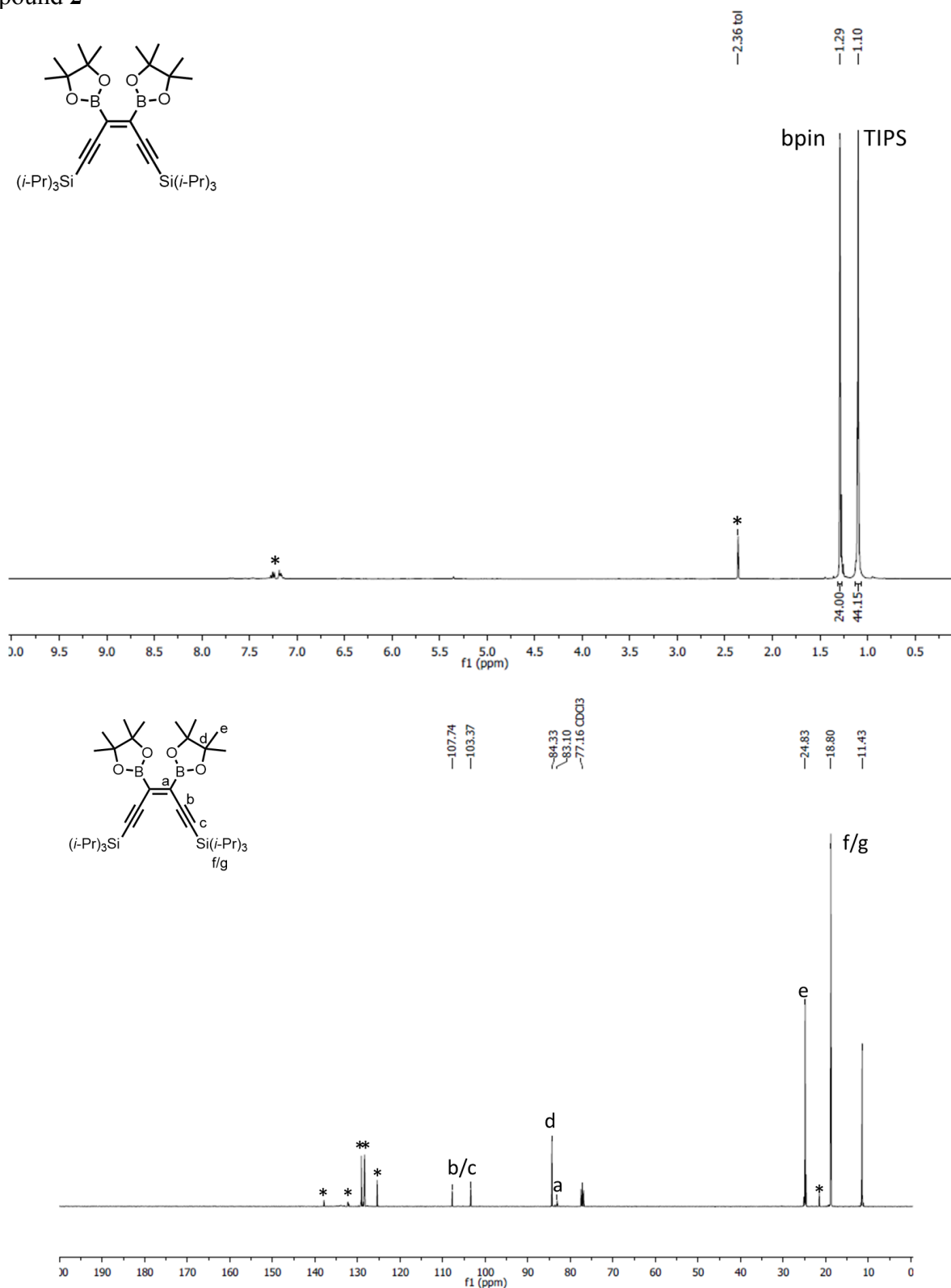



**Figure S10.** $^1$H NMR (400 MHz, CDCl$_3$, 294 K) and $^{13}$C NMR (101 MHz, CDCl$_3$, 294 K) spectra of **2**. * Residual toluene and PPh$_3$ signals are present as the product is not stable on silica.
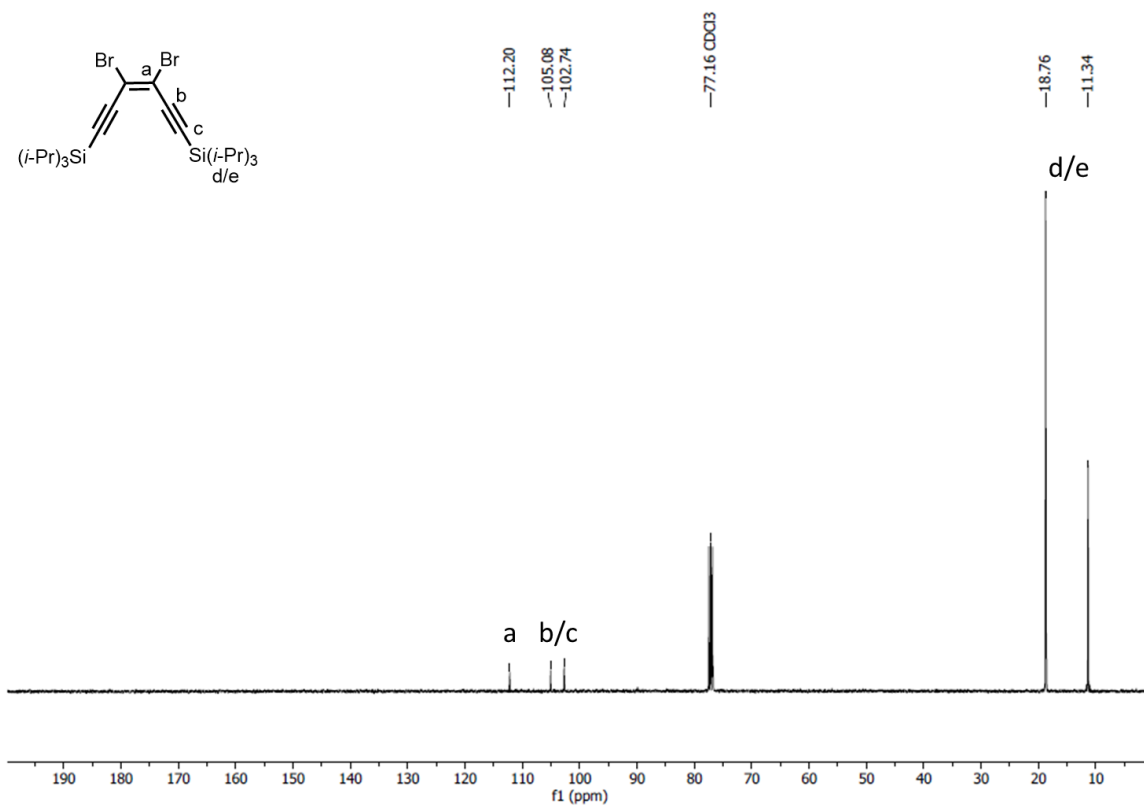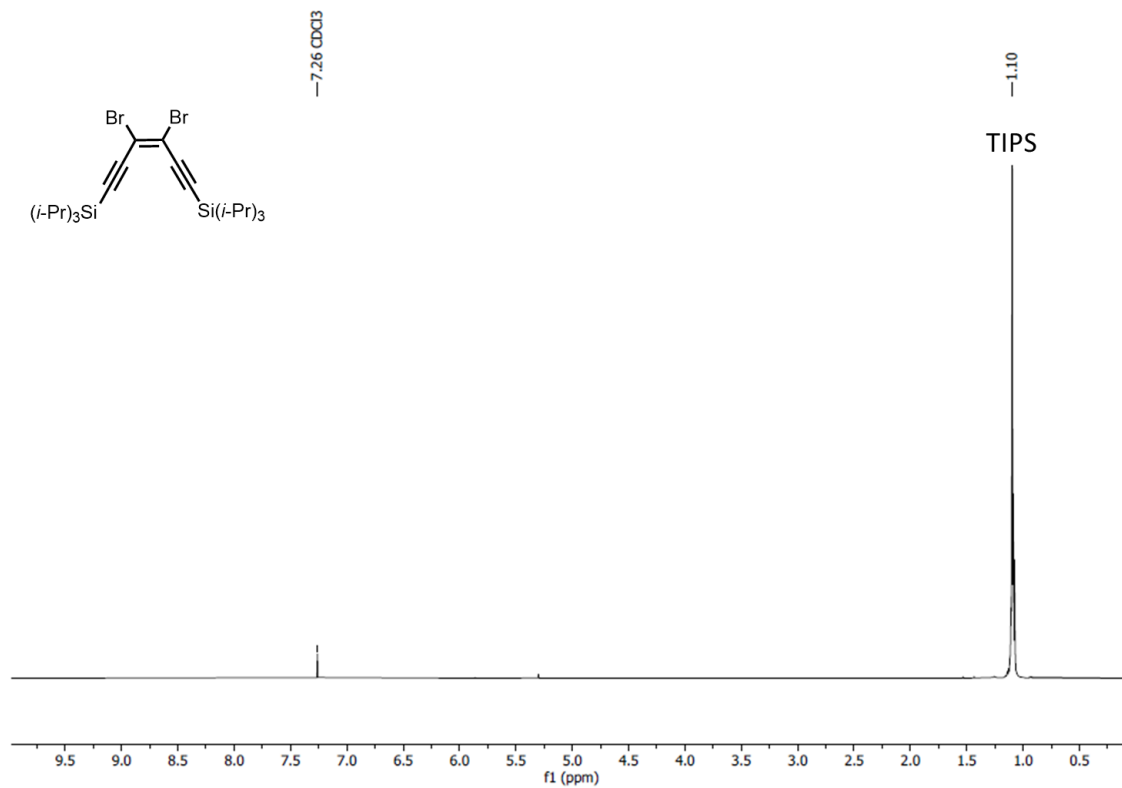
Compound **3**





**Figure S11.** $^1$H NMR (400 MHz, CDCl$_3$, 294 K) and $^{13}$C NMR (101 MHz, CDCl$_3$, 294 K) spectra of **3**.
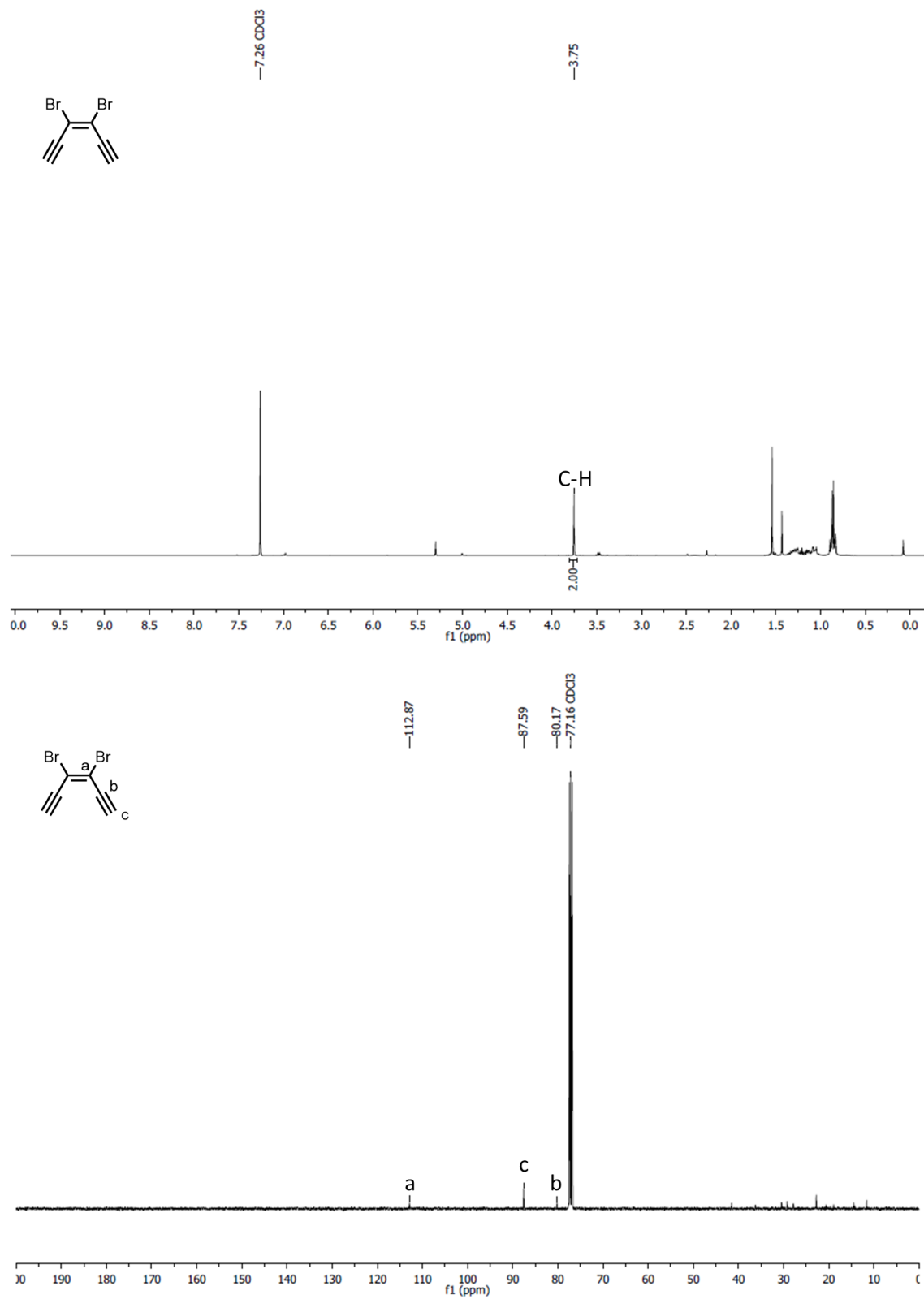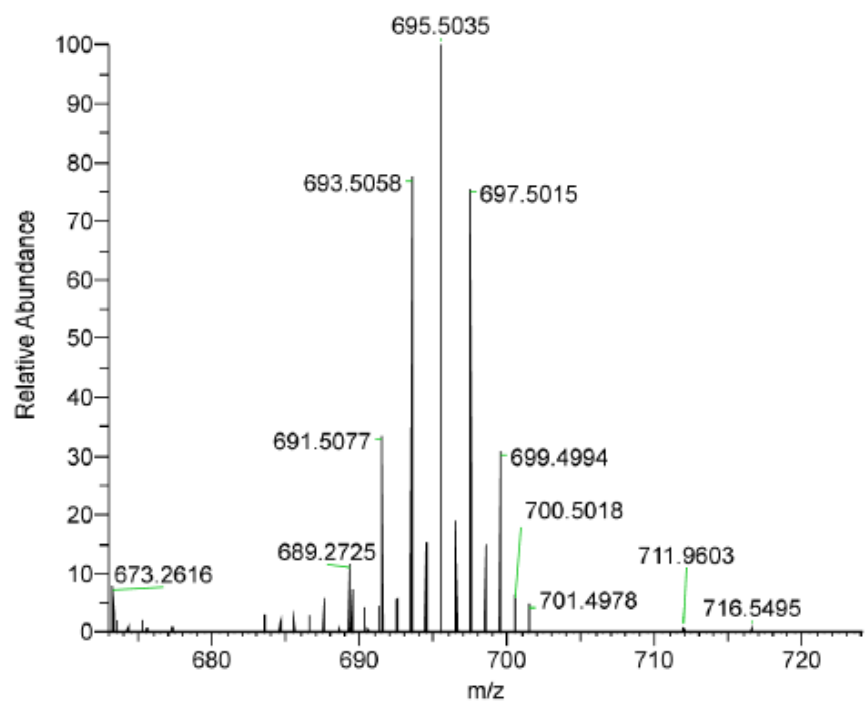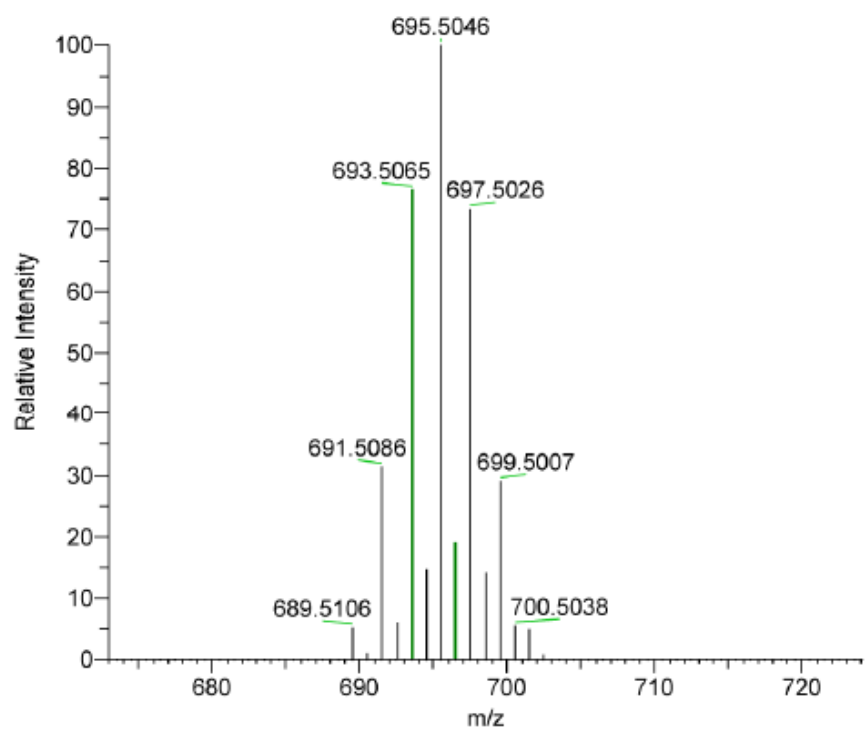
Compound **4**





**Figure S12.** ¹H NMR (400 MHz, CDCl₃, 294 K) and ¹³C NMR (101 MHz, CDCl₃, 294 K) spectra of **4**. Residual petroleum ether signals are present as the sample was not completely dried to avoid decomposition.

**C$_{18}$Br$_6$**



**Figure S13.** Mass spectrum of the radical M$^-$ ion of C$_{18}$Br$_6$ detected in APCI.

## Section 10: References

1. Jones, G. B.; Wright, J. M.; Plourde, G. W.; Hynd, G.; Huber, R. S.; Mathews, J. E. A Direct and Stereocontrolled Route to Conjugated Enediynes. *J. Am. Chem. Soc.* **2000**, *122*, 1937–1944.

2. Solas, M.; Suárez-Pantiga, S.; Sanz, R. Ethyl lactate as a renewable carbonyl source for the synthesis of diynones. *Green Chem.* **2019**, *21*, 213–218.

3. Kohn, D. R.; Gawel, P.; Xiong, Y.; Christensen, K. E.; Anderson, H. L. Synthesis of Polyynes Using Dicobalt Masking Groups. *J. Org. Chem.* **2018**, *83*, 2077–2086.

4. Cosier, J.; Glazer, A. M. A nitrogen-gas-stream cryostat for general X-ray diffraction studies. *J. Appl. Cryst.* **1986**, *19*, 105–107.

5. Sheldrick, G. M. *SHELXT* – Integrated space-group and crystal-structure determination. *Acta Cryst.* **2015**, *A71*, 3–8.

6. (a) Parois, P.; Cooper, R. I.; Thompson, A. L. Crystal structures of increasingly large molecules: meeting the challenges with CRYSTALS software. *Chem. Cent. J.* **2015**, *9*, 30. (b) Cooper, R. I.; Thompson, A. L.; Watkin, D. J. *J. Appl. Cryst.* **2010**, *43*, 1100–1107.

7. Giessibl, F. J. High-Speed Force Sensor for Force Microscopy and Profilometry Utilizing a Quartz Tuning Fork. *Appl. Phys. Lett.* **1998**, *73*, 3956–3958.

8. Albrecht, T. R.; Grütter, P.; Horne, D.; Rugar, D. Frequency Modulation Detection Using High-Q Cantilevers for Enhanced Force Microscope Sensitivity. *J. Appl. Phys.* **1991**, *69*, 668–673.

9. Bennewitz, R.; Barwich, V.; Bammerlin, M.; Loppacher, C.; Guggisberg, M.; Baratoff, A.; Meyer, E.; Güntherodt, H. J. Ultrathin Films of NaCl on Cu(111): A LEED and Dynamic Force Microscopy Study. *Surf. Sci.* **1999**, *438*, 289–296.

10. Repp, J.; Meyer, G.; Rieder, K.-H. Snell's Law for Surface Electrons: Refraction of an Electron Gas Imaged in Real Space. *Phys. Rev. Lett.* **2004**, *92*, 036803.

11. L. Bartels, L.; Meyer, G.; Rieder, K.-H. Controlled vertical manipulation of single CO molecules with the scanning tunneling microscope: A route to chemical contrast. *Appl. Phys. Lett.* **1997**, *71*, 213–215.

12. Gross, L.; Mohn, F.; Moll, N.; Liljeroth, P.; Meyer, G. The Chemical Structure of a Molecule Resolved by Atomic Force Microscopy. *Science* **2009**, *325*, 1110–1113.

13. Stipe, B.; Rezaei, M.; Ho, W.; Gao, S.; Persson, M.; Lundqvist, B. Single-molecule dissociation by tunneling electrons. *Phys. Rev. Lett.* **1997***, 78*, 4410–4413.

14. Kim, Y.; Komeda, T.; Kawai, M. Single-molecule reaction and characterization by vibrational excitation. *Phys. Rev. Lett., APS* **2002***, 89*, 126104

15. Ladenthin, J. N.; Grill, L.; Gawinkowski, S.; Liu, S.; Waluk, J.; Kumagai, T. Hot Carrier-Induced Tautomerization within a Single Porphycene Molecule on Cu (111). *ACS Nano* **2015**, *9*, 7287–7295.

16. Schendel, V.; Borca, B.; Pentegov, I.; Michnowicz, T.; Kraft, U.; Klauk, H.; Wahl, P.; Schlickum, U.; Kern, K. Remotely Controlled Isomer Selective Molecular Switching. *Nano Lett.* **2016**, *16*, 93–97.

17. Pavliček, N.; Majzik, Z.; Collazos, S.; Meyer, G.; Pérez, D.; Guitian, E.; Peña, D.; Gross, L. Generation and Characterization of a Meta-Aryne on Cu and NaCl Surfaces. *ACS Nano*, **2017**, *11*, 10768–10773.

18. Kaiser, K.; Scriven, L. M.; Schulz, F.; Gawel, P.; Gross, L.; Anderson, H. L. An *sp*-Hybridized Molecular Carbon Allotrope, Cyclo[18]carbon. *Science* **2019**, *365*, 1299–1301.

19. Pavliček, N.; Gawel, P.; Kohn, D. R.; Majzik, Z.; Xiong, Y.; Meyer, G.; Anderson, H. L.; Gross, L. Polyyne formation via skeletal rearrangement induced by atomic manipulation. *Nat. Chem.* **2018**, *10*, 853–858.

20. Rapenne, G.; Grill, L.; Zambelli, T.; Stojkovic, S.; Ample, F.; Moresco, F.; Joachim, C. Launching and landing single molecular wheelbarrows on a Cu (1 0 0) surface. *Chem. Phys. Lett.* **2006***, 431*, 219–222.

21. Zhang, Y.; Schuler, B.; Fatayer, S.; Gross, L.; Harper, M. R.; Kushnerick, J. D. Understanding the effects of sample preparation on the chemical structures of petroleum imaged with noncontact atomic force microscopy. *Ind. Eng. Chem. Res.* **2018***, 57*, 15935–15941.

22. Hapala, P.; Kichin, G.; Wagner, C.; Tauz, F. S.; Temirov, R.; Jelínek, P. Mechanism of high-resolution STM/AFM imaging with functionalized tips. *Phys. Rev. B* **2014**, *90*, 085421.

23. van der Lit, J.; Di Cicco, F.; Hapala, P.; Jelinek, P.; Swart, I. Submolecular Resolution Imaging of Molecules by Atomic Force Microscopy: The Influence of the Electrostatic Force. *Phys. Rev. Lett.* **2016**, *116*, 096102.

24. Arulmozhiraja, S.; Ohno, T. CCSD Calculations on $C_{14}$, $C_{18}$, and $C_{22}$ Carbon Clusters. *J. Chem. Phys.* **2008**, *128*, 114301.

25. Blum, V.; Gehrke, R.; Hanke, F.; Havu, P.; Havu, V.; Ren, X.; Reuter, K.; Scheffler, M. *Ab initio* molecular simulations with numeric atom-centered orbitals. *Comput. Phys. Commun.* **2009**, *180,* 2175–2196.

26. Heyd, J.; Scuseria, G. E. Hybrid functionals based on a screened Coulomb potential, *J. Chem. Phys.* **2003**, *118*, 8207–8215.

25. Tkatchenko, A.; Scheffler, M. Accurate Molecular Van Der Waals Interactions from Ground-State Electron Density and Free-Atom Reference Data. *Phys. Rev. Lett.* **2009**, *102*, 073005.